Climate Dynamics
https://doi.org/10.1007/s00382-023-07093-y

ORIGINAL ARTICLE

Atmospheric responses to the interannual variability of sea surface temperature front in the summertime Southern Ocean

Qian-Rong Rao[1] · Li Zhang[2,3] · Xuya Ren[2,3] · Lixin Wu[2,3]

Received: 5 September 2023 / Accepted: 25 December 2023

Abstract
Air–sea interactions in mid-latitudes and their climatic effects have long been a research focus. However, the influence of the variability of the Southern Oceanic Front (SOF) on atmospheric processes at interannual timescales remains somewhat ambiguous from existing studies. Using reanalysis data, our findings reveal that the SOF reaches its maximum intensity during the austral summer, characterized by pronounced interannual variability and an insignificant trend. On the one hand, an enhanced SOF intensifies the meridional temperature gradient and atmospheric baroclinicity, accompanied by increased local and downstream baroclinic energy conversion. This amplifies storm track activities in both the lower and upper troposphere. On the other hand, the atmospheric circulation in mid- and high-latitudes exhibits an equivalent barotropic response. This is attributed to the feedback of storm tracks on the mean flow, dominated by the transient eddy vorticity forcing. Moreover, we compare the relative contributions of the South Indian Oceanic Front (SIOF) and South Atlantic Oceanic Front (SAOF) variability to storm track and atmospheric circulation. Results indicate that the SIOF variability dominates the downstream development of storm track response and modulates the anomalous atmospheric circulation around the Antarctic, while the SAOF variability produces only a limited local atmospheric response.

Keywords Mid-latitude air–sea interaction · Oceanic fronts · Storm track · Atmospheric circulation · Eddy-mean flow feedback

1 Introduction

In midlatitudes, oceanic frontal zones are key areas for air-sea interactions (Czaja and Frankignoul 1999; Kushnir et al. 2002; Minobe et al. 2008; Kwon et al. 2010; Wills and Thompson 2018). Sea surface temperature (SST) anomalies have a substantial impact on storm-track activity as well as the intensity or meridional movement of eddy-driven jets (Lorenz and Hartmann 2001; Lee and Kim 2003; Robinson 2006), particularly within the mid-latitude oceanic front zones (Nakamura et al. 2004; Small et al. 2014; O'Reilly and Czaja 2015; Parfitt et al. 2016). In accordance with the oceanic baroclinic adjustment mechanism, the oceanic fronts exhibit asymmetrical sensible heat flux contributions along their warm and cold sides, thus facilitating the transport of eddy heat flux towards the polar regions. This promotes the preservation of the atmospheric temperature gradient and baroclinity near the surface (Eady 1949). The robust baroclinity is conducive to synoptic-scale transient eddies and maintains a close association with storm tracks and westerly jets, which appear to be firmly influenced by oceanic fronts acting as an anchoring role (Nakamura and Shimpo 2004; Taguchi et al. 2009; Ogawa et al. 2012). Nakamura et al. (2008) revealed the significant impact of midlatitude oceanic fronts on storm tracks through a comparative numerical experiment wherein meridional SST gradients were either retained or eliminated. The experimental results denote that the removal of the midlatitude meridional SST gradient induces notable attenuation in both upper and lower tropospheric storm track intensity. At the same time, the surface westerly winds induced by transient eddies are also greatly weakened. This indicates that the strong meridional SST gradient prevalent within the oceanic front zone plays

✉ Li Zhang
zhangli@ouc.edu.cn

[1] College of Meteorology and Oceanography, National University of Defense Technology, Changsha, China

[2] Frontiers Science Center for Deep Ocean Multispheres and Earth System and Key Laboratory of Physical Oceanography, Ocean University of China, Qingdao, China

[3] Laoshan Laboratory, Qingdao, China

Published online: 03 February 2024

a crucial role in anchoring the position and strength of the storm track and eddy-driven jets, which is further substantiated through high-resolution regional patterns (Nonaka et al. 2009; Taguchi et al. 2009; Sampe et al. 2010; Small et al. 2014).

In the North Pacific, both the subtropical front zone (STFZ) and the subarctic front zone (SAFZ) have a close relationship to the midlatitude storm track and atmospheric circulation, and has garnered sustained attention (Nakamura et al. 2004; Nakamura and Yamane 2010; Taguchi et al. 2012; Wang et al. 2019). Frankignoul et al. (2011) argued that the meridional migration of SAFZ engenders a barotropic atmospheric response with a lag of 2 months. Kuwano-Yoshida and Minobe (2017) found that the emergence of positive geopotential height anomalies over the Okhotsk Sea and Gulf of Alaska consequent to the presence of the SAFZ. Some studies have pointed out the close connection between the subtropical front and the Pacific Decadal Oscillation (PDO) (Mantua et al. 1997; Mantua and Hare 2002; Wang et al. 2019). They found that years characterized by strong (weak) STFZ are accompanied by SST anomalies that align with the warm (cold) phase of the PDO, which leads to a strengthening (weakening) of the baroclinity in the lower atmosphere, thereby exerting an influence on the upper atmosphere. In addition, Chen et al. (2019) found that STFZ greatly leads to changes in storm tracks and westerly jet in mid latitude regions by inducing the vertical propagation of baroclinic Rossby waves and influencing the frequency of barotropic Rossby wave breaking events. Based on observation and analysis of changes in the North Pacific air-sea system, the meridional SST gradient anomaly and its accompanying atmospheric transient eddy-dynamic feedback are considered as one of the key processes in the mid-latitude unstable air-sea interaction (Fang and Yang 2016; Wang et al. 2019; Zhang et al. 2020a). The response of atmospheric circulation anomalies displays an equivalent barotropic structure vertically, where in areas of low pressure coincide with colder SSTs, and areas of high pressure align with warmer SSTs (Kushnir et al. 2002; Namias and Cayan 1981; Cayan 1992; Deser and Blackman 1993; Fang and Yang 2016). In the North Atlantic, studies also have found that the Gulf Stream front considerably amplifies the intensity of the storm track within the lower troposphere concurrently prompting a barotropic response (Minobe et al. 2008; Small et al. 2014; O'Reilly et al. 2017; Wills and Thompson 2018).

Similar mechanisms and processes might also be active in the variability of oceanic frontal zones influencing the atmosphere in the Southern Hemisphere (SH), which have been less studied. Due to the strong high-frequency variability of fronts on both spatial and temporal scales, it is difficult to obtain a large number of sample data through traditional in situ observations (Hopkins et al. 2008), and thus there are multiple criteria to define fronts in the Southern Ocean. As a result, different definitions can have a significant impact on results, which is of particular importance for the study of variability and change (Graham et al. 2012; Chapman et al. 2020). In fact, the utilization of SST gradients to detect fronts in the Southern Ocean presents an effective approach for examining both the position and the seasonal variation of these fronts (Chapman et al. 2020), and a number of studies have been conducted to analyze Southern Ocean fronts using SST data (Kostianoy et al. 2004; Moore et al. 1999; Freeman et al. 2016). For the atmosphere, numerous studies have shown that the storm track in the SH occurs in a banded structure in the region between 40°–60° S, with the maximum of the storm track moving from the Atlantic across the Indian Ocean to the Pacific, and the distribution of the storm track in summer and autumn is circular, while in winter and spring is somewhat asymmetric, with variations accompanied by background westerly jet (Simmonds and Keay 2000; Lim and Simmonds 2002; Hoskins and Hodges 2005; Chemke et al. 2022). Ogawa et al. (2016) explored the possible influence of mid-latitude oceanic frontal zones on the characterization of the winter SH barotropic annular mode by conducting several sets of idealized "aqua-planet" experiments with zonally uniform oceanic frontal zones. Through methodically altering the latitude of frontal gradients in SST profiles, it is observed that the characterization of the wintertime annular mode displays a pronounced sensitivity to the position of SST fronts within both mid-latitude and subpolar latitudes. Using the same "aqua-planet" experiments, a recent study also revealed that the midlatitude oceanic frontal zone restores near-surface baroclinicity, thereby amplifying and anchoring the variability of baroclinic annular mode in SH (Nakayama et al. 2021). However, the exploration of the processes and mechanisms by which the interannual variability of mid-latitude SST fronts in the SH affects the storm tracks and atmospheric circulation, as well as the relative contributions of fronts in different ocean basins, remains an unresolved issue in observations.

The study aims to explore the dynamic processes and mechanisms of the impact of SST front variability on the mid-latitude atmosphere in the Southern Ocean, focusing on how SST fronts induce storm track anomalies, which in turn lead to a response in the atmospheric circulation through transient eddies. The paper is organized as follows. The data and methods are introduced in Sect. 2. Section 3 shows the seasonal variation of SST front in the Southern Ocean. Section 4 investigates the processes and mechanisms responsible for how the SST fronts affect the storm track and atmospheric circulations. Sections 5 and 6 give a discussion and summary, respectively.

2 Data and methods

In this study, austral summer (DJF) refers to December, January and February. SST and atmospheric variables including static air temperature (T), geopotential height (Z), sea surface pressure (SLP) and atmospheric horizontal and vertical wind speed (u, v, ω) used in this study are from the fifth generation European Center for Medium Range Weather Forecasts reanalysis (ERA5) dataset for 1979–2020. The data has a horizontal resolution of 0.25°×0.25° and 37 vertical pressure levels from 1000 to 10 hPa.

We use the meridional eddy heat flux ($v'T'$) at 850 hPa and meridional wind speed variance ($v'v'$) at 250 hPa to characterize the storm track at midlatitude in the SH (Chang et al. 2002; Yin 2005; Nakamura et al. 2008; Taguchi et al. 2009). Here prime represents the synoptic-scale (2–8 days) transient disturbance. Besides, according to Lindzen and Farrell (1980), we estimate atmospheric baroclinic instability by using the maximum Eady growth rate, which is expressed as $\sigma_{BI} = 0.31\mathrm{gN}^{-1}\theta^{-1}|\partial\theta/\partial y|$, where θ represents the potential temperature and N represents the Brunt–Väisälä frequency. We also diagnose the local baroclinic energy conversion (BCEC), including BCEC1 and BCEC2. BCEC1 represents the baroclinic energy conversion from mean available potential energy (MAPE) to eddy available potential energy (EAPE), and BCEC2 represents the baroclinic energy conversion from EAPE to eddy kinetic energy (EKE). The specific expressions are as follows:

$$BCEC(MAPE\ to\ EAPE) = -C_1\left(\frac{P_0}{P}\right)^{\frac{R_d}{C_p}}\left(-\frac{d\theta}{dp}\right)^{-1}\left(\overline{u'T'}\frac{\partial\bar{T}}{\partial x}+\overline{v'T'}\frac{\partial\bar{T}}{\partial y}\right)$$

$$BCEC(EAPE\ to\ EKE) = -C_1\overline{\omega'T'}$$

where $C_1 = (\frac{P_0}{P})^{\frac{C_v}{C_p}}\frac{R}{g}$, P_0=1000 hpa, R refers to the gas constant, g is the acceleration of gravity, C_p and C_v are the specific heat capacity of dry air at constant volume and constant pressure, respectively; the remaining notations are consistent with the previous definition. Prime also denotes the synoptic-scale (2–8 days) transient disturbance and overbar denotes the seasonal-mean (Cai et al. 2007).

Prior to the data analysis, we use multiple linear regression to remove the influence of the tropical ENSO. Following the method adopted by Ren et al. (2022) and Zhang et al. (2023), time series of the first and second modes of the SSTA field in the tropical Pacific region (170.5° W–120.5° W, 5.5° N–5.5° S) which were derived by using empirical orthogonal function (EOF) analysis were used as the main characteristic time series Z(t) of the ENSO. Then, the portion affected by Z(t) is subtracted from the original field $\xi^*(x, y, t)$ to obtain the new field ξ with the ENSO signal removed by using the formula: $\xi = \xi^* - Z \times \frac{cov(\xi^*, Z)}{var(Z)}$. In this paper, each variable is preprocessed to linearly remove the effects of ENSO and the variables are seasonally averaged.

To evaluate the variations of SST front in the Southern Ocean under global warming, monthly outputs from 44 CMIP6 models are analyzed over the span of 1900–2099. These models are initially subjected to historical anthropogenic and natural forcings until 2014, followed by simulations under the future greenhouse-gas forcing associated with the SSP5–8.5 emission scenario extending to 2100 (Eyring et al. 2016). Given the limited number of CMIP6 models, we employ a bootstrap method to assess the statistical significance of the multi-model mean decrease in the intensity of the Southern Indian Ocean Front (SIOF). Specifically, the 44 intensity values of SIOF from 1900 to 1999 (represented by blue bars in Fig. 14) undergo random resampling to generate 10,000 realizations of a multi-model mean across the 44 models. During this resampling process, any given value may be selected more than once. This same procedure is replicated for the 2000–2099 period (represented by red bars in Fig. 14). The standard deviation of the 10,000 realizations of the mean value is calculated for both periods. If the difference in the multi-model mean values between the two periods exceeds the sum of the respective standard deviation values from the 10,000 realizations, the difference is deemed statistically significant at the 95% confidence level.

3 Seasonal variation of SST front in the Southern Ocean

The large-scale SST fronts in the Southern Ocean are identified by calculating the SST meridional gradient (∂SST/∂y) (Chapman et al. 2020), and the absolute values of the gradient reflect the intensity of the fronts. The climatological seasonal mean SST meridional gradient (Fig. 1) show that the SST fronts in Southern Ocean distribute with a meridional range of about 35°–60° S throughout the whole year and their intensity can reach up to more than 2 °C/100 km. The spatial structure of the fronts is much more complex than that of the Kuroshio and the Gulf Stream. The fronts in the South Atlantic and the western part of the South Indian Ocean are strong, while the fronts in the South Pacific are quite weak and are difficult to characterize. Regardless of the seasons, the intensity of the fronts is largest in the region from 60° W to 120° E. Therefore, we select the SST fronts in this region to be defined as the Southern Oceanic Front (SOF) for further study.

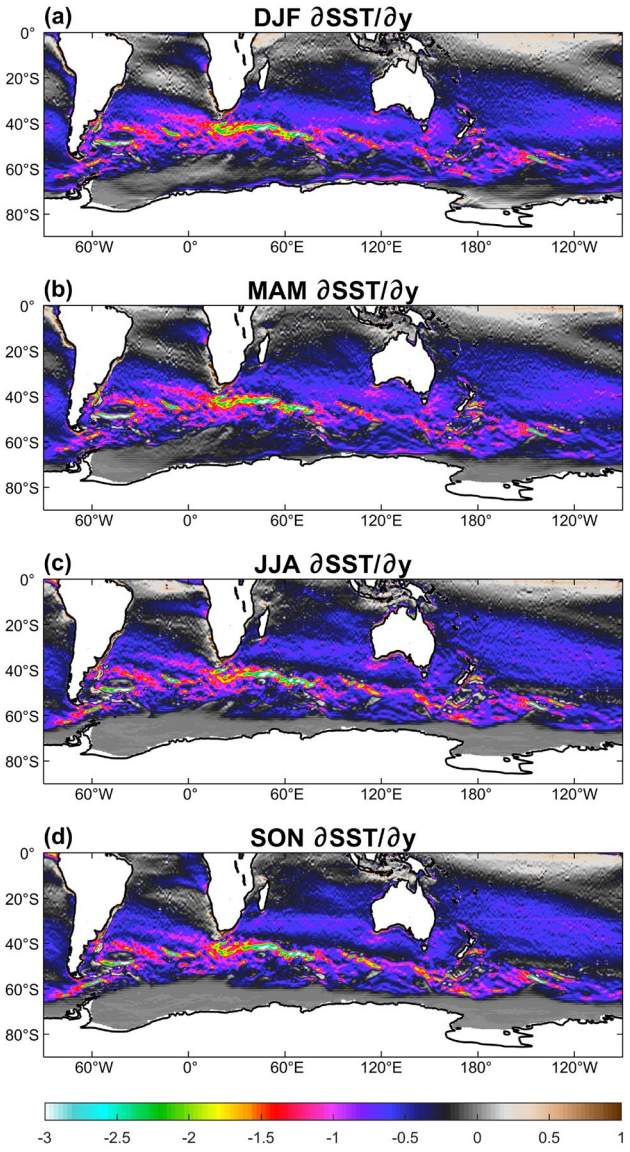

Fig. 1 Climatological distribution of SST meridional gradient (∂SST/∂y, units: °C/100 km) in Southern Ocean during **a** summer (DJF), **b** autumn (MAM), **c** winter (JJA), **d** spring (SON)

We start by analyzing the seasonal variability of the SOF, as show in Fig. 2. Results of zonally-averaged SST meridional gradient show that the SOF is stronger and wider range in the warm season than in the cold season (Fig. 2a). The index to quantify the oceanic frontal intensity can be obtained by zonally-averaged SST meridional gradient within the frontal zone. The specific formula is as follows (e.g., Wang et al. 2019; Zhang et al. 2020a):

$$ITS = \sum_{i=1}^{N} G_i/N$$

where G_i is the value of zonally-averaged SST meridional gradient that is no less than an empirically-given critical value (here, 0.8 °C/100 km for SOF) at the i-th latitudinal grid point within the zone, and N is the number of total grid points that satisfy the criteria above. The intensity index reflects an average of the SST meridional gradient within the frontal zone. It can be seen that the frontal intensity (Fig. 2b) and variability (Fig. 2d) of SOF reaches its strongest in austral summer (DJF), without a significant trend. In other seasons, the frontal intensity of SOF is relatively weaker, with a significant positive trend. Further power spectrums show that, except for JJA, there are enhanced variance on the interannual timescales with a coherent peak of 8-year in other seasons (Fig. 2c). Thus, we will focus on the SOF variation in the summer period.

The influence of various ocean basins on the atmosphere may exhibit non-local effects. Particularly in the SH midlatitudes, the prevalent westerly acts as a waveguide. That is, downstream development mechanism (e.g., Chang et al. 2002; Orlanski and Chang 1993; Zhang et al. 2020a) and eddy-mean flow interactions (e.g., Fang and Yang 2016; Zhang et al. 2023) in this region may lead to a notably pronounced atmospheric response in the downstream side of oceanic frontal zones. Considering this, it is necessary to emphasize the relative contributions of SST fronts within different ocean basins to atmospheric response. We divide the SOF into the South Indian Oceanic Front (SIOF) and the South Atlantic Oceanic Front (SAOF), with latitudinal ranges of about 0°–85° E and 60° W–0°, respectively. The intensity index of SIOF and SAOF are defined in the same way as above (Fig. 2a), and 0.8 °C/100 km is still chosen as the empirically-given critical value for the two fronts. For the SIOF, three different frontal longitudinal ranges (0°–85° E, 15°–85° E and 30°–85° E) are selected for the definition of the frontal intensity index (Fig. 3a), and it is found that the change of the frontal range of SIOF will not affect its frontal intensity as well as the subsequent results, so only the discussion of SIOF with latitudinal range of 15°–85° E is presented next. Figure 3b shows the time series of the intensity index of SOF, SIOF and SAOF, and it is clear that the intensity of SIOF in the summer period is larger than that of SAOF.

Figure 4a shows the spatial distribution of SST anomalies regressed upon the intensity index of SOF, and it can be seen that SST anomaly is positive to the north of 45° S and negative to the south of 45° S in the SOF region. This dipole distribution of SST anomalies is typically accompanied by an increased SST meridional gradient. Figure 4b and c show partial regressions of SST upon the normalized intensity index of SIOF and SAOF. The distribution of SST anomalies corresponding to the SIOF variability exhibits a cooling along 45° S toward the polar side and warming towards the equatorial side. And SST anomaly

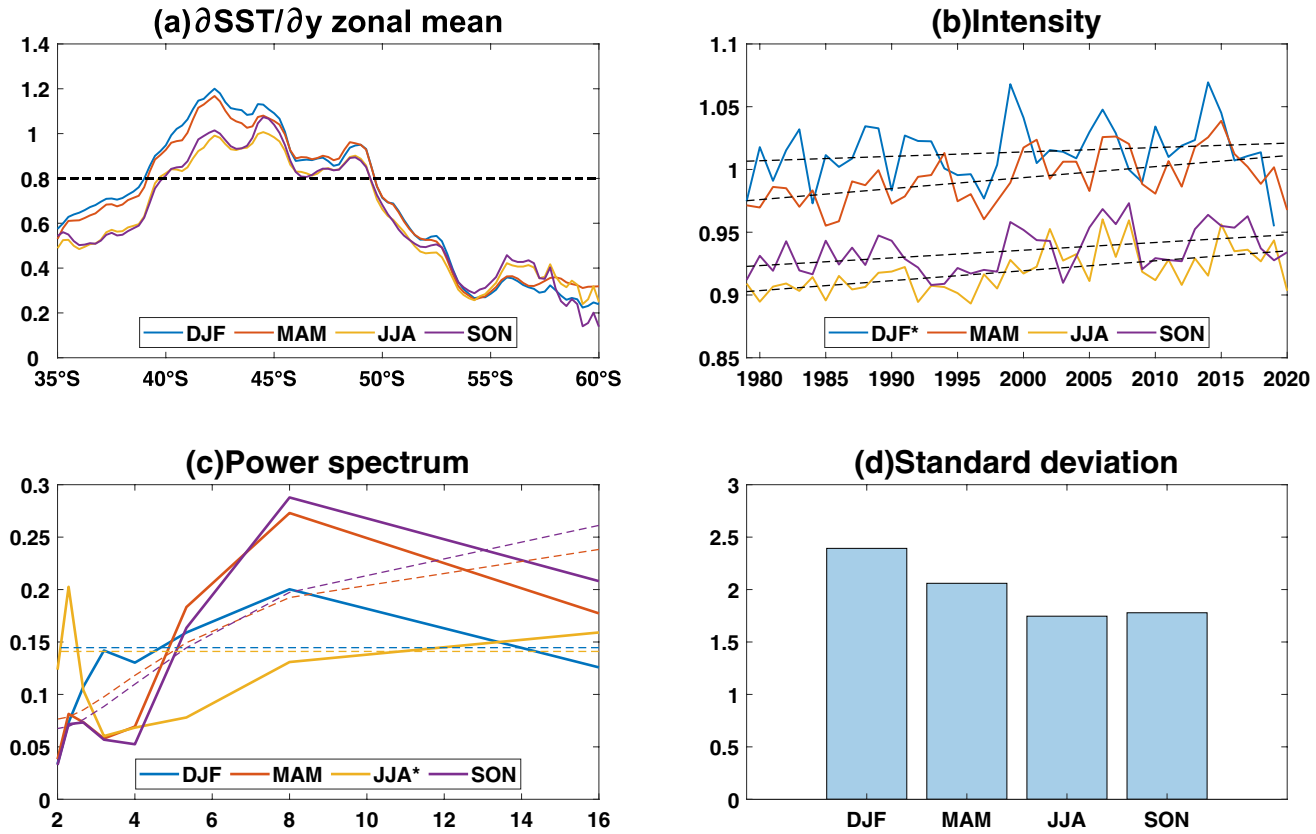

Fig. 2 **a** Climatological SST meridional gradient (units: °C/100 km) zonally-averaged over 60° W–120° E, i.e., the region of SOF. **b** Time series of seasonal intensity index of SOF (solid lines; units: °C/100 km) with trends (dashed lines). **c** Power spectrum and **d** standard deviation of time seasonal intensity index of SOF. Levels of 95% statistical confidence (dashed lines) are indicated in **c**

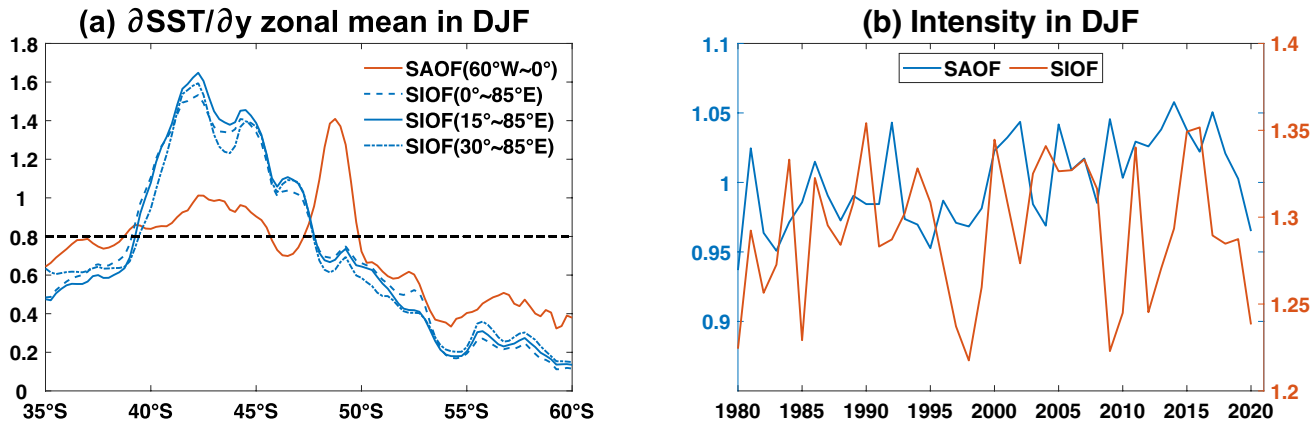

Fig. 3 **a** Climatological SST meridional gradient (units: °C/100 km) zonally-averaged over the regions of SAOF (orange line) and SIOF (blue line) in summer (DJF), with the horizontal black dashed line denoting the empirically-given critical value. **b** Time series of the intensity index of SAOF (blue line) and SIOF (orange line) for the summer period (DJF)

corresponding to the SAOF variability along 50° S exhibits a dipole structure of warming in the north and cooling in the south. It becomes evident that the boundaries of positive and negative SST anomalies coincide with the positions of their corresponding fronts. Notably, although the SAOF is weaker than the SIOF, their associated SST anomalies are of comparable magnitude, suggesting that both the SAOF and SIOF could potentially have significant impacts on the atmosphere (Zhang et al. 2021).

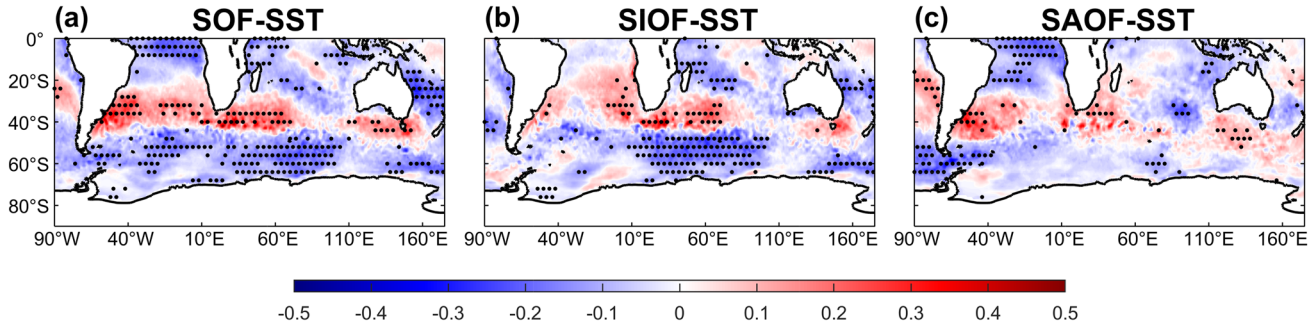

Fig. 4 Regressions of SST (units: °C) onto the normalized intensity indexes of **a** SOF, **b** SIOF, **c** SAOF in summer, where **b** and **c** are partial regressions. And the intensity indexes are detrended before normalization. Black dots indicate the regions where the confidence level is larger than 95%

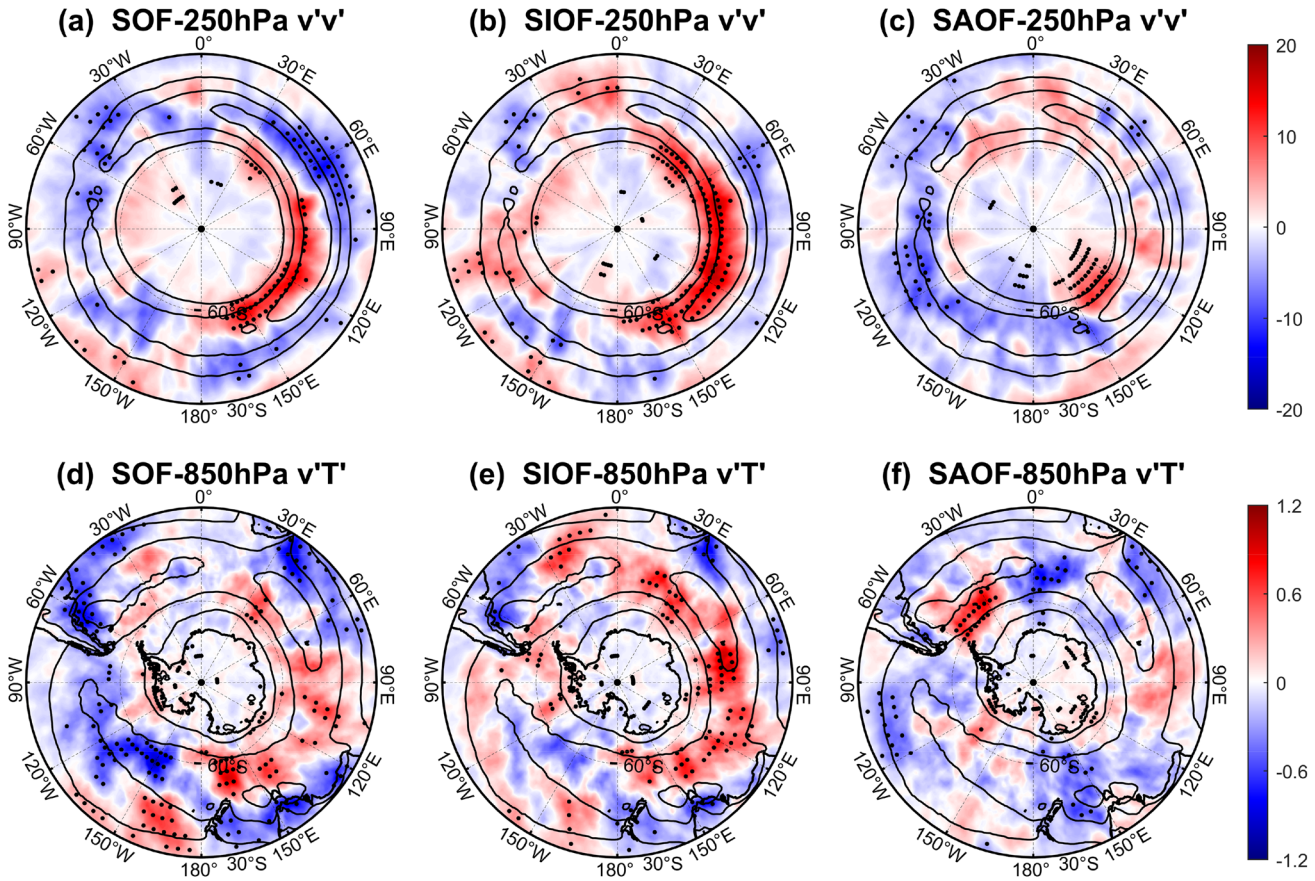

Fig. 5 The horizontal distributions of the climatologies (contours) and the atmospheric anomalies (shading) regressed upon the normalized intensity indexes of SOF (left), SIOF (center), SAOF (right) for **a**–**c** $\langle v'v' \rangle$ (units: $m^2\ s^{-2}$) at 250 hPa, **d**–**f** $\langle v'T' \rangle$ (units: K m s^{-1}) at 850 hPa in summer, where **b** and **c**, **e** and **f** are partial regressions. And the intensity indexes are detrended before normalization. The contour interval is 50 $m^2\ s^{-2}$ for **a**–**c**, and 4 K m s^{-1} for **d**–**f**. Black dots indicate the regions where the confidence level is larger than 95%

4 Impacts of the SST fronts on summertime storm track and large-scale atmospheric circulations in the SH

4.1 Impacts of storm track and corresponding baroclinic processes

The climatological distribution of the storm track in the lower troposphere (Fig. 5d–f, contours) shows that there are two peaks over the South Indian Ocean and the South Atlantic with zonal ranges of 30°–90° E and 60° W–0°, respectively, and the maximum amplitude is up to 10 K m s^{-1}. The two centers of maximum of storm track coincide with the positions of SIOF and SAOF (recall Fig. 1a), while the strength of storm track over the South Pacific is relatively weaker, with an amplitude of about 6 K m s^{-1}. Besides, the storm track in the upper troposphere (Fig. 5a–c, contours) basically shows a circumpolar distribution, with a peak over the South Indian Ocean. Regardless of the upper and lower troposphere, the storm-track activities over the South Pacific is relatively weak, and we know that the SST fronts in the South Pacific are weak. The position correspondence between storm tracks and oceanic frontal zones for the mean state reflects the "anchoring" of large-scale SST fronts on the storm tracks and eddy-driven jets, which has been demonstrated by previous studies based on idealized models.

The patterns of the storm track anomalies in the lower troposphere shows the spatial distribution of 850-hPa $<v'T'>$ anomaly regressed upon the intensity index of SOF (Fig. 5d), and it can be seen that there is a positive anomaly toward the pole from 60° W eastward to 180°, with maximum response of 1.2 K m s^{-1}, inducing a poleward enhancement of storm-track activities. The pattern of $v'T'$ anomaly induced by SIOF variability (Fig. 5e) is similar to that induced by SOF, but the meridional width of the region where the storm track anomalies are positive is larger than that in Fig. 5d. The strong positive anomaly response of the storm track ($v'T'$) to the SAOF variability is concentrated in the western South Atlantic, with a negative anomaly response in the eastern South Atlantic. In the lower troposphere, the enhancements of SOF and SIOF lead to the poleward transport of eddy heat flux over the frontal zone (0° eastward to 90° E) and its downstream side (90° E eastward to 180°). In the upper troposphere, the strong response of positive $<v'v'>$ anomaly induced by SOF variability (Fig. 5a) is also concentrated in downstream side (30° E eastward to 150° E), so the storm-track activity is consistently strengthened in both the lower and upper troposphere. The SIOF variability also dominate the response of the storm track in the upper troposphere (Fig. 5b), which is similar to anomalous responses induced by the SOF variability, while the storm track anomaly induced by the SAOF variability is not significant (Fig. 5c). The above analyses indicate that the responses of storm track in both the lower and upper troposphere are characterized by downstream development, and the SIOF variability plays a dominant role in the influence of SST front variability on storm track.

Next, we diagnose the change in the atmospheric baroclinic instability, which serves as a baroclinic source for the growth of storm track (Eady 1949; Chang et al. 2002). Climatologically, $\partial T/\partial y$ and σ_{BI} over the South Atlantic and South Indian Ocean are stronger than that over the South Pacific, corresponding to the positions and intensities of SST fronts (Fig. 6, contours). The strong $\partial T/\partial y$ and σ_{BI} are observed over South America, which are led by the topography (The Andes; Zhang et al. 2021). When SST fronts intensify, the meridional temperature gradients increase (Fig. 6a–c), corresponding to an increase in atmospheric baroclinity (Fig. 6d–f). It can be observed that $\partial T/\partial y$ and σ_{BI} anomalies exhibit consistency, and σ_{BI} anomalies caused by SOF and SIOF variability have a similar structure, both of which cause changes of atmospheric baroclinicity in the frontal zones (Fig. 6d, e). Although the intensity and range of SAOF are relatively small compared to the SIOF (recall Fig. 1), the strength and range of the maximum Eady growth rate in response to SAOF variability is slightly larger (Fig. 6e, f).

The downstream development of synoptic eddies is a well-known character for the storm tracks, which features a series of coherent baroclinic wave packets propagating along the westerly jet (Lee and Held 1993; Zhang et al. 2020b). The downwind development of new packets is attributed to energy transfer by the upwind packets via the ageostrophic geopotential fluxes. The propagation of coherent baroclinic wave packets can be illustrated by a longitude-time diagram with the squared eddy meridional wind anomalies for any given month or season and is not sensitive to the year chosen. Take the summers of 1990 and 2010 (Fig. S1a, b) for example, we can clearly see that coherent baroclinic wave packets travelling eastward along the 50° S parallel for one or more circles. Similar patterns can also be observed in other years (not shown). We estimate the packets group velocity and the eddies phase speed using a one-point correlation. The group velocity is greater than the phase velocity, indicating downstream development process (Fig. S1c). As mentioned above, there is a significant positive anomalous response of the maximum Eady growth rate due to SAOF variability, but we only see a significant enhancement in the storm track response in local South Atlantic in the lower troposphere, which seems to indicate that changes in SST fronts and atmospheric baroclinicity in the South Atlantic are not able to have a significant impact on circumpolar storm-track activities through an effective "downstream development" mechanism.

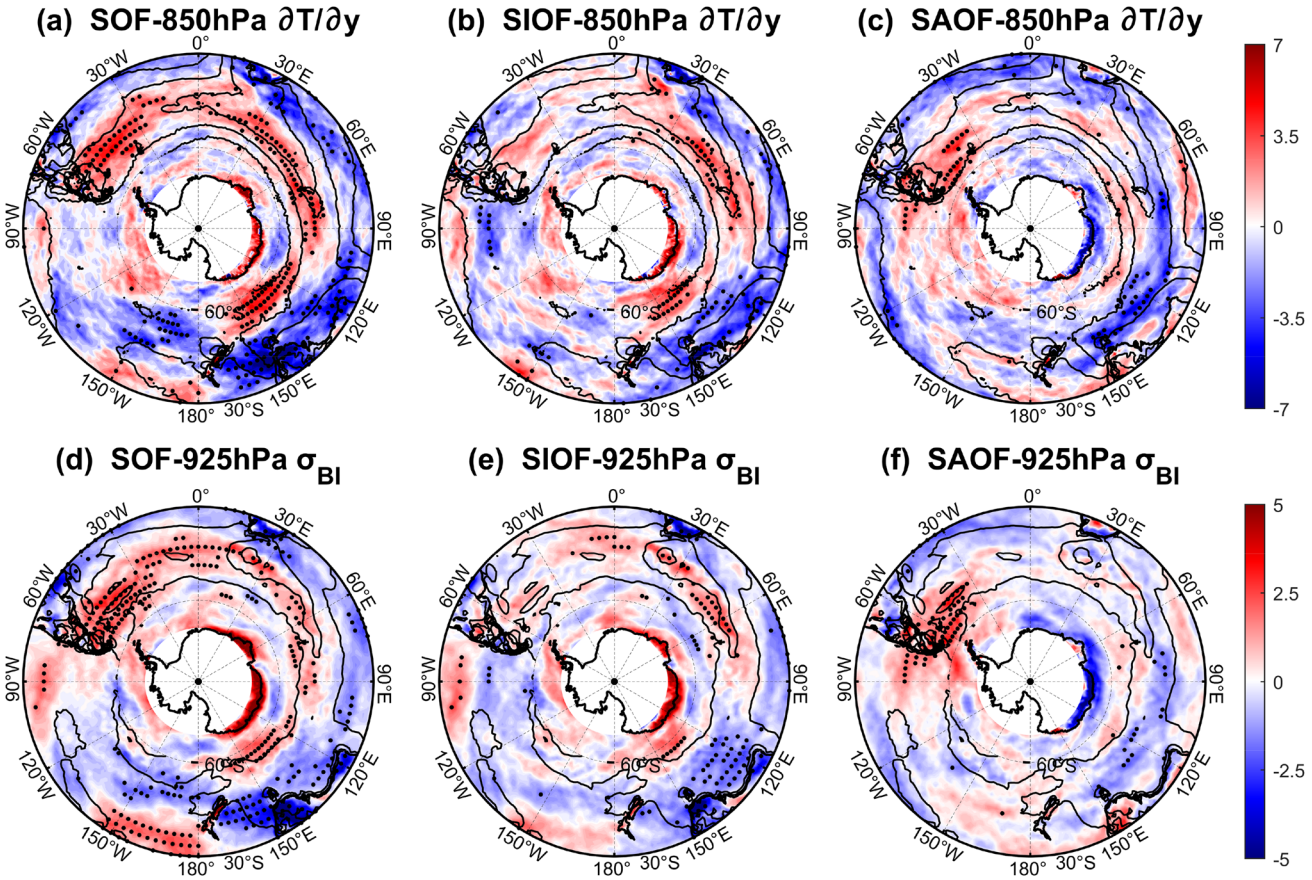

Fig. 6 The horizontal distributions of the climatologies and the atmospheric anomalies (shading) regressed upon the normalized intensity indexes of SOF (left), SIOF (center), SAOF (right) for **a**–**c** air temperature gradient ($\partial T/\partial y$, units: 10^{-2} °C/100 km) at 850 hPa, **d**–**f** maximum Eady growth rate σ_{BI} (units: 10^{-2} day^{-1}) at 925 hPa in summer, where **b** and **c**, **e** and **f** are partial regressions. And the intensity indexes are detrended before normalization. The contour interval is 0.2 °C/100 km for **a**–**c**, and 0.2 day^{-1} for **d**–**f**. Black dots indicate the regions where the confidence level is larger than 95%

For the energetic perspective, the lost energy due to the barotropic decay and dissipation can be regained by the effective baroclinic energy conversion (BCEC) on the downstream side of the synoptic eddies which facilitates the downstream propagation without significant weakening (Chang and Orlanski 1993). Thus, we diagnose BCEC, including BCEC1 (the energy conversion from MAPE to EAPE) and BCEC2 (the energy conversion from EAPE to EKE), to evaluate the effective utilization of atmospheric baroclinic instability energy by storm track. BCEC1 and BCEC2 anomalies regressed upon the intensity indexes of fronts are exhibited with shading of Fig. 7. When the intensity of SOF and SIOF increase, BCEC1 and BCEC2 are significantly enhanced over the South Atlantic and South Indian Ocean (Fig. 7a, b, d, e), while the enhancement of SAOF causes BCEC1 and BCEC2 to be strengthened only over the western South Atlantic (Fig. 7c, f). And BCEC1 and BCEC2 anomalies induced by SOF and SIOF exhibit similar response towards downstream. Furthermore, the promotion of baroclinic energy conversion leads to the development of synoptic eddies, indicating continuous strengthening of storm-track activities.

4.2 Impacts of atmospheric circulation associated with transient eddy activities

The geopotential height anomalies regressed upon the intensity index of SOF show a circumpolar response with negative anomalies in the polar regions and positive anomalies along the mid-latitudes (Fig. 8a, d, g), corresponding to the intensified westerly jet around the pole when SOF becomes stronger (Fig. 9a, d, g). It can be noted that zonal wind is intensified where there is a large gradient of geopotential height anomalies. More importantly, the geopotential height and zonal westerly wind anomalies exhibits the same structures in the lower, middle, and upper troposphere, suggesting that the atmospheric circulation responds to the SOF variability with a barotropic atmospheric vertical structure. Furthermore, the geopotential height and westerly jet patterns partially regressed upon the intensity index of SIOF (Figs. 8b, e, h

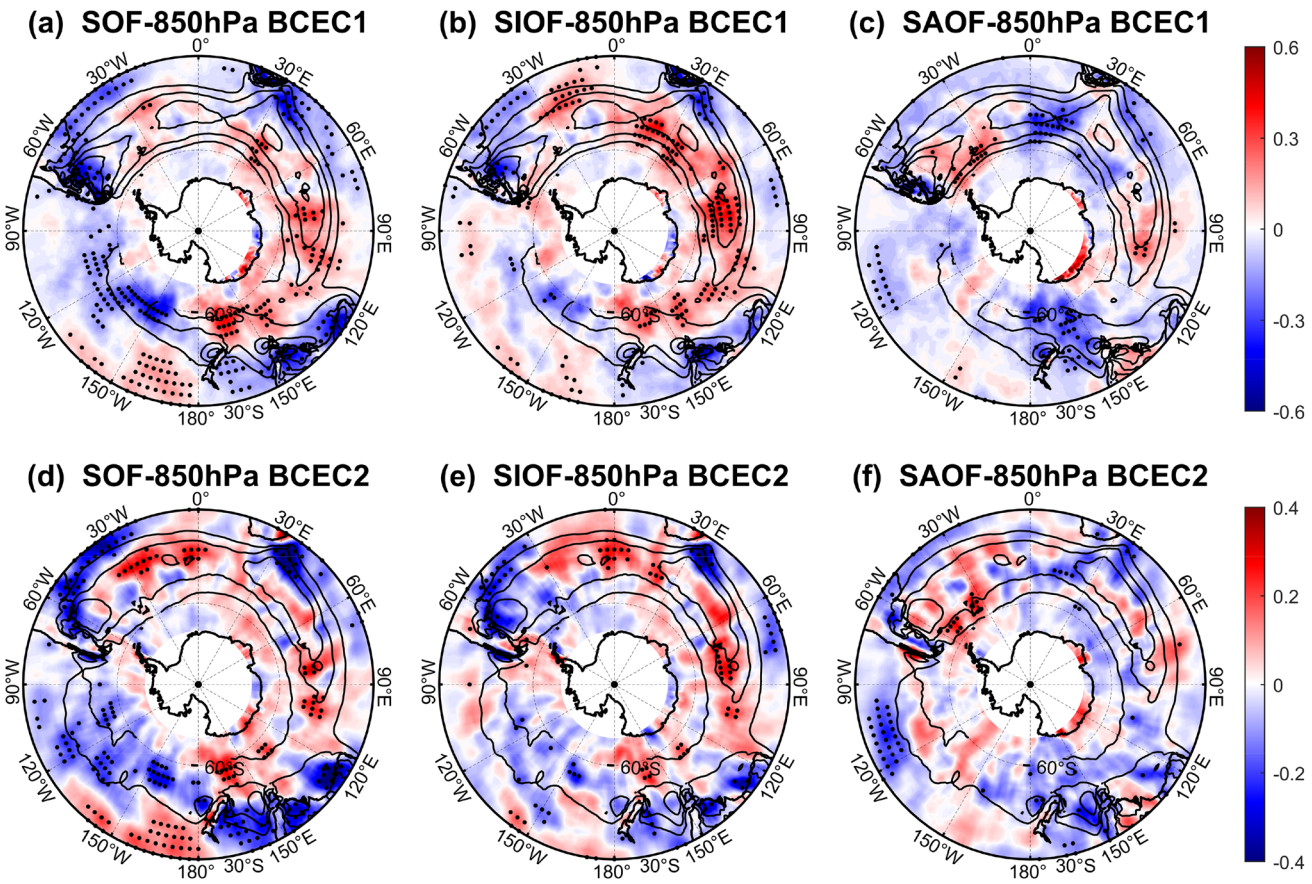

Fig. 7 The horizontal distributions of the climatologies (contours; interval 1 W m^{-2}) and the atmospheric anomalies (shading) regressed upon the normalized intensity indexes of SOF (left), SIOF (center), SAOF (right) for local baroclinic energy conversion from **a**–**c** MAPE to EAPE (BCEC1, units: W m^{-2}), **d**–**f** EAPE to EKE (BCEC2, units: W m^{-2}) at 850 hPa in summer, where **b** and **c**, **e** and **f** are partial regressions. And the intensity indexes are detrended before normalization. Black dots indicate the regions where the confidence level is larger than 95%

and 9b, e, h) are quite similar to those regressed upon the intensity index of SOF (Figs. 8a, d, g and 9a, d, g), whereas the atmospheric anomalies caused by the SAOF variability (Figs. 8c, f, i and 9c, f, i) are quite weak and less significant. Therefore, it suggested that SIOF acts as a dominated role in the influence of fronts in the Southern Ocean on atmospheric circulation during austral summertime.

At mid-latitudes, the atmosphere is characterized by westerly jet and associated transient eddies which can redistribute heat and momentum in the atmosphere, thereby driving and maintaining atmospheric circulation. Based on quasi-geostrophic potential vorticity (QGPV) equation (Lau and Holopainen 1984), the geopotential height tendency ($\partial\overline{Z}/\partial t$) induced by synoptic-scale transient eddies can be evaluated with the following equation (Nishii et al. 2009; Fang and Yang 2016):

$$\left[\nabla^2 + f^2\frac{\partial}{\partial p}\left(\frac{1}{\sigma}\frac{\partial}{\partial p}\right)\right]\frac{\partial\overline{Z}}{\partial t} = -\frac{f}{g}\nabla\cdot\overline{\mathbf{V}_h'\zeta'} + \frac{f^2}{g}\frac{\partial}{\partial p}\left[-\frac{\alpha}{\sigma}\frac{\nabla\cdot\overline{\mathbf{V}_h'T'}}{T}\right]$$

where $\sigma = -\alpha\theta^{-1}(\partial\theta/\partial p)$ is the static stability parameter, α is the specific volume, θ is the potential temperature; f is Coriolis parameter, V_h is the atmospheric horizontal wind speed, ζ is the relative vorticity, and the remaining notations are consistent with the previous definition; prime also denotes the synoptic-scale (2–8 days) transient disturbance and overbar denotes the seasonal-mean. On the right side of the equation, $\overline{Q_{eddy}} = -\nabla\cdot\overline{\mathbf{V}_h'T'}$ is the transient eddy heating forcing, representing the convergence of heat flux transport by transient eddies, and $\overline{F_{eddy}} = -\nabla\cdot\overline{\mathbf{V}_h'\zeta'}$ is the transient eddy vorticity forcing, which represents the convergence of vorticity flux transport by transient eddies. $\partial\overline{Z}/\partial t$ signifies the geopotential height tendency caused by transient eddy thermal forcing ($\overline{Q_{eddy}}$) and dynamic forcing ($\overline{F_{eddy}}$). Thus, transient eddy activities can have an effect on atmospheric circulation by transporting heat and vorticity fluxes.

From the climatological view, the heat flux transported by transient eddies (Q_{eddy}) converges south of 50° S and diverges north of 50° S (Fig. 10a), which indicates that the atmospheric transient eddy activities always tend to

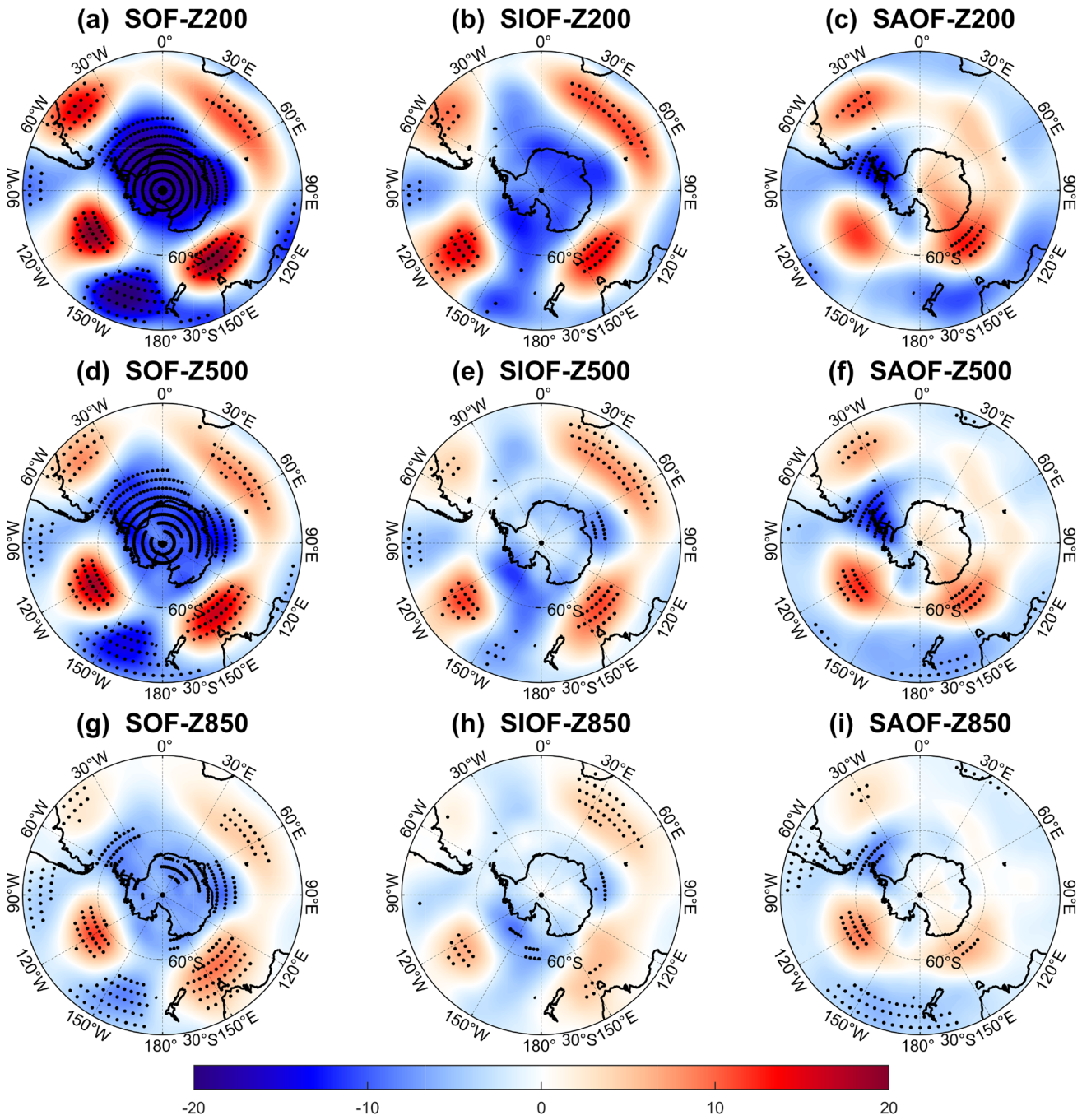

Fig. 8 Regressions of geopotential height (units: m) onto the normalized intensity indexes of SOF (left), SIOF (center), SAOF (right) at **a**–**c** 200 hPa, **d**–**f** 500 hPa, and **g**–**i** 850 hPa in summer, where **b** and **c**, **e** and **f**, **h** and **i** are partial regressions. And the intensity indexes are detrended before normalization. Black dots indicate the regions where the confidence level is larger than 95%

transport heat from low latitude to high latitude, that is, the polarward transport of eddy heat. And the vorticity flux transported by transient eddies (F_{eddy}) is a potential vorticity source of the seasonal-mean atmosphere. In Fig. 10e, F_{eddy} has an equivalent barotropic structure, with negative values south of 50° S and positive values north of 50° S. Thus, the meridional dipole type distribution of F_{eddy} tends to maintain a westerly jet near 50° S.

The Q_{eddy} and F_{eddy} anomalies are in phase with their corresponding climatology. The Q_{eddy} anomaly caused by the SOF variability has a baroclinic structure in the vertical direction and the largest response in the upper troposphere (Fig. 10b), which suggests that enhancement

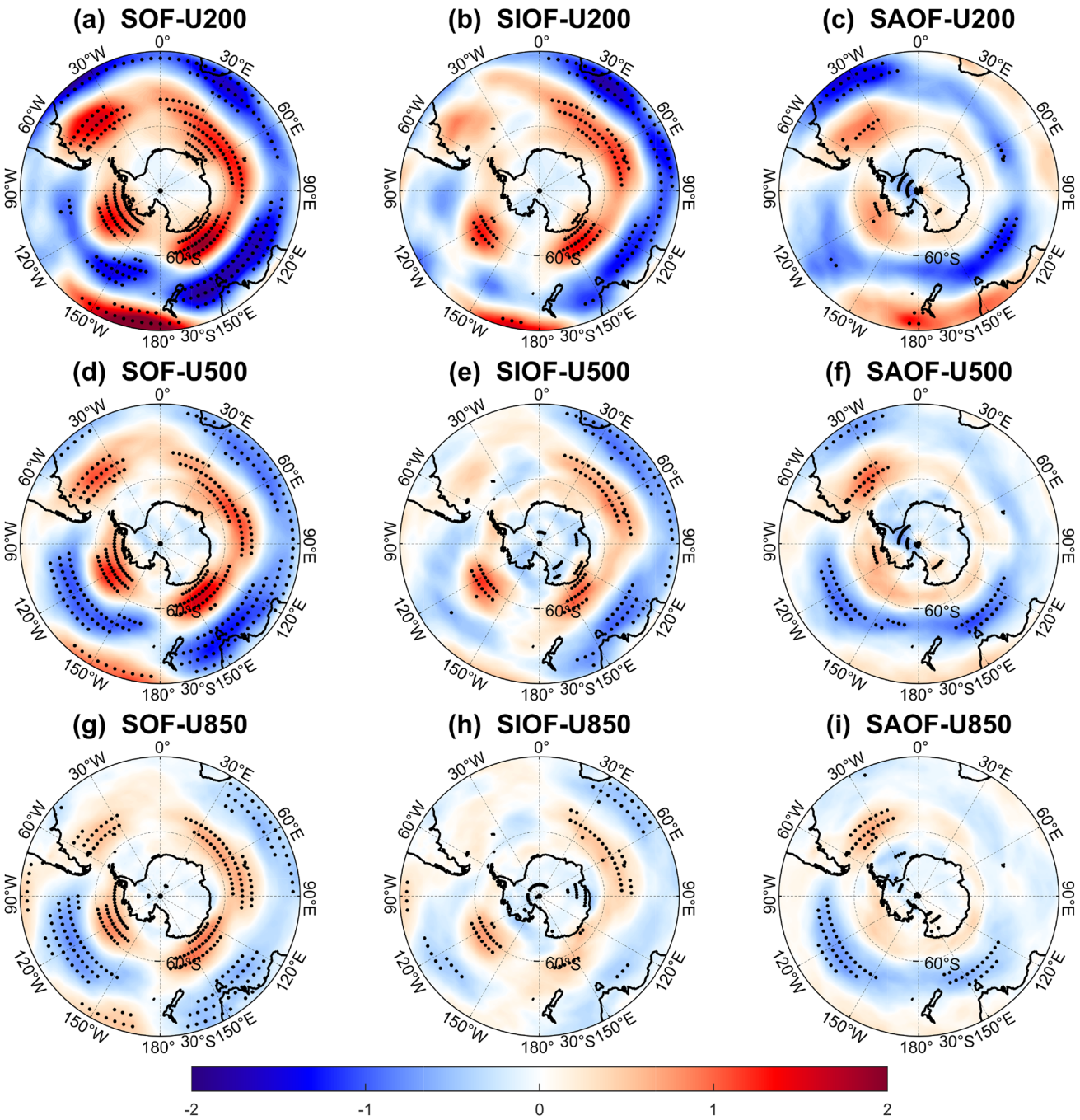

Fig. 9 Regressions of zonal wind velocity (units: m/s) onto the normalized intensity indexes of SOF (left), SIOF (center), SAOF (right) at **a**–**c** 200 hPa, **d**–**f** 500 hPa, and **g**–**i** 850 hPa in summer, where **b** and **c**, **e** and **f**, **h** and **i** are partial regressions. And the intensity indexes are detrended before normalization. Black dots indicate the regions where the confidence level is larger than 95%

of SOF promotes poleward heat flux transport by mid-to-high latitude transient eddies. F_{eddy} exhibits an anomalous response with a barotropic structure, where convergence increases north of 60° S and weakens south of 60° S (Fig. 10f). The climatology distribution of F_{eddy} indicates that the westerly jet axis is located near 50° S, while the maximum gradient of F_{eddy} anomaly occurs at 60° S. This indicates that the enhancement of SOF will promote the poleward strengthening of westerly winds, causing the jet axis to move southward. Besides, it can be found that the Q_{eddy} and F_{eddy} anomalies induced by SIOF variability and SOF variability present basically consistent spatial distributions (Fig. 10c, g), while Q_{eddy} and F_{eddy} anomalies caused by the SAOF variability (Fig. 10d, h) are weaker.

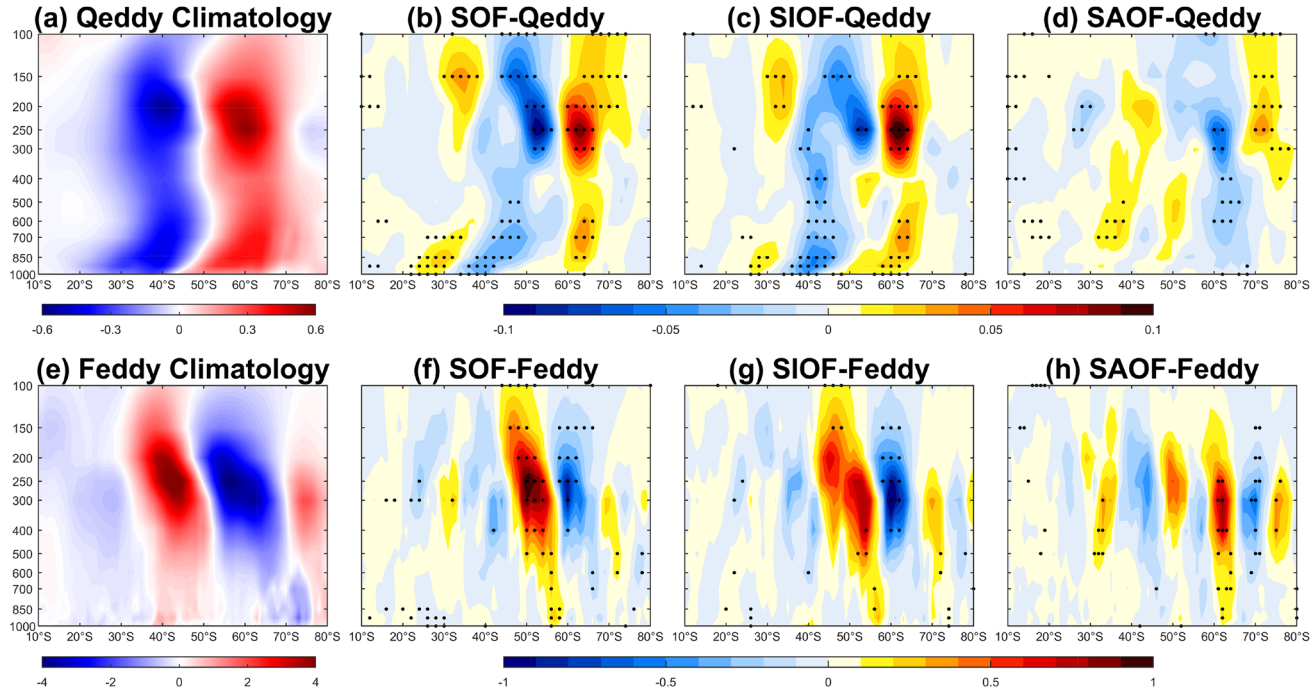

Fig. 10 Latitude–altitude sections of **a**, **b** climatologies and **c**, **d**, **f**–**h** anomalies zonally-averaged over 0°–180° regressed upon the normalized intensity indexes of SOF (second column), SIOF (third column), SAOF (last column) for Q_{eddy} (upper panels, units: 10^{-5} K s^{-1}) and F_{eddy} (lower panels, units: 10^{-11} s^{-2}), where **e** and **d**, **g** and **h** are partial regressions. And the intensity indexes are detrended before normalization. Black dots indicate the regions where the confidence level is larger than 95%

Accordingly, the SST fronts in Southern Ocean can influence the westerly jet through synoptic-scale transient eddies, and the process is dominated by the SIOF variability in austral summer.

Next, we use geopotential height tendency equation to calculate geopotential height tendency caused by the transient eddy thermal forcing, the transient eddy vorticity forcing and both forcings, and regressed onto the normalized intensity indexes of SOF, SIOF, SAOF. It becomes apparent that the total geopotential height tendency anomalies (the third column in Fig. 11; Fig. 12) caused by these three fronts variabilities are barotropic. And the barotropic F_{eddy} anomalies caused by frontal variabilities can lead to anomalous responses in geopotential height tendency with barotropic structure, with stronger responses in the upper troposphere (the second column in Fig. 11; Figs. S2 and S3). Compared with the geopotential height tendency anomalies caused by Q_{eddy} with baroclinic structure (the first column in Fig. 11; Figs. S2 and S3), F_{eddy} plays a more important role in generating and maintaining the equivalent barotropic atmospheric anomalies. Moreover, it can be noticed that geopotential height tendency anomalies induced by SOF and SIOF variability are basically the same, and there are a large range of positive anomalies around the pole in the mid-latitudes, compared with the small impact of SAOF variability on geopotential height tendency. Combining the geopotential height anomaly field caused by frontal variability in Fig. 8, the maximum area of geopotential height tendency positive anomalies basically corresponds to where the geopotential height anomalies are positive, that is, the change of geopotential height tendency caused by frontal variabilities mainly contribute to the area of geopotential height positive anomalies, and then strengthens the anticyclone circulation in mid-latitude region, correspondingly increasing the westerly jet. In addition, it can be seen that the maximum of geopotential height tendency anomalies can reach 3.5 m/day (Figs. 11, 12), so it takes about 7–8 days to form the geopotential height responses as shown in Fig. 8.

5 Discussion

5.1 Weakened SST fronts in the future climate

Since 1950, about 90% of the growing heat resulting from greenhouse warming has been taken in the ocean (Levitus et al. 2005). Notably, in the span from 2005 to 2014, the Southern Ocean has contributed to more than 60% of the overall increase in global ocean heat content (Durack et al. 2014; Wijffels et al. 2016). The Southern Ocean has experienced considerable warming, with projections indicating further warming, but remain uncertain (Cai et al. 2023).

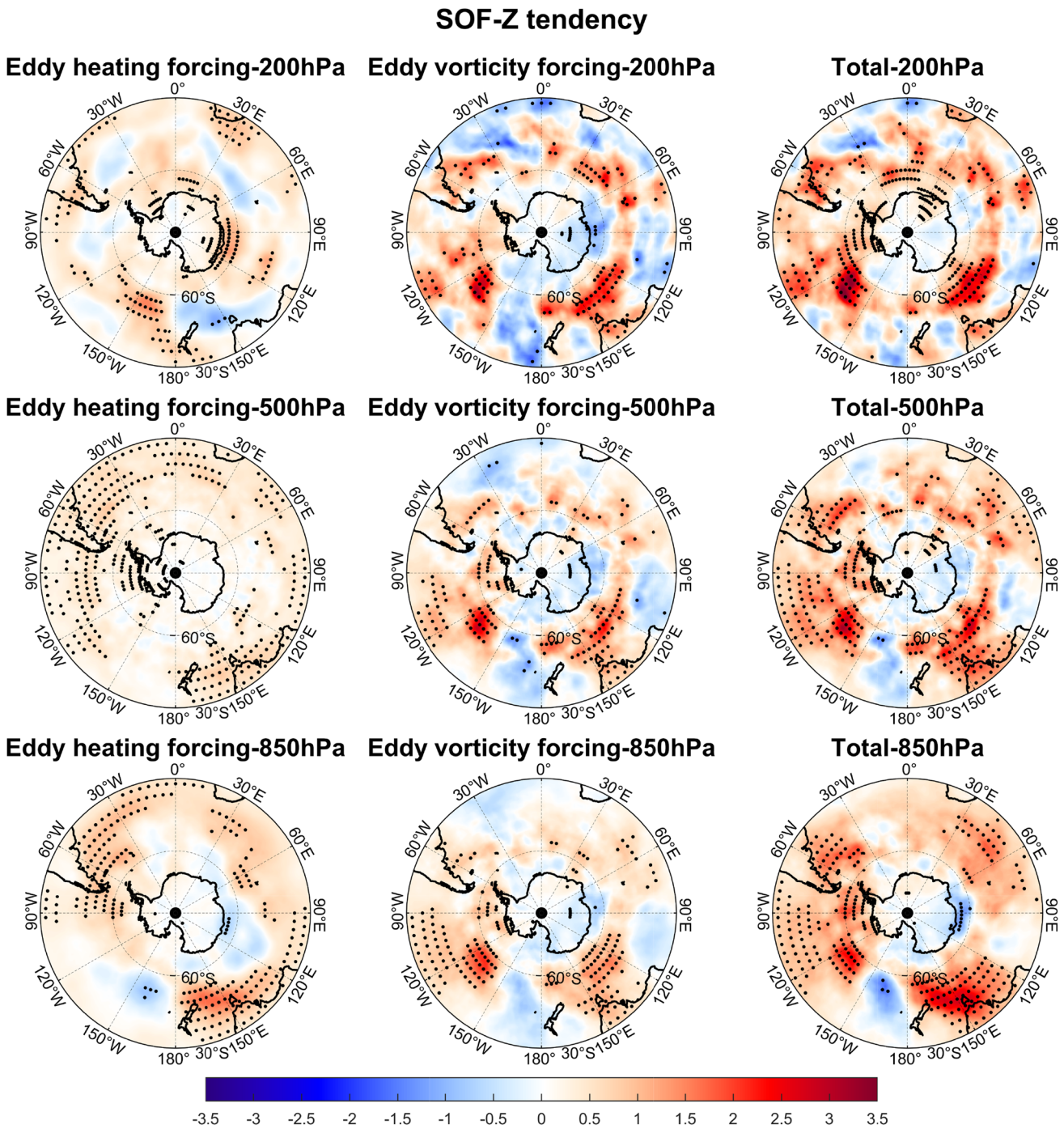

Fig. 11 Regressions onto the normalized intensity index of SOF of geopotential height tendency (units: m/day) induced by transient eddy vorticity forcing (left), transient eddy heating forcing (center), and the sum of these two forcings (right) at 200 hPa (top), 500 hPa (middle), and 850 hPa (bottom) in summer. And the intensity index is detrended before normalization. Black dots indicate the regions where the confidence level is larger than 95%

An open question arises as to how SST fronts changes in the Southern Ocean under global warming. To shed a bit more light on this issue, we utilize SST outputs from the CMIP6 models to calculate the SST meridional gradients during summer in the present-day (1970–1999) and future (2070–2099) periods, and their differences (future − present), as shown in Fig. 13. The red (blue) color in Fig. 13c represents positive (negative), which means that the absolute value of the gradient decreases (increases), i.e., the frontal intensity is weakened (strengthened). It can be seen that the

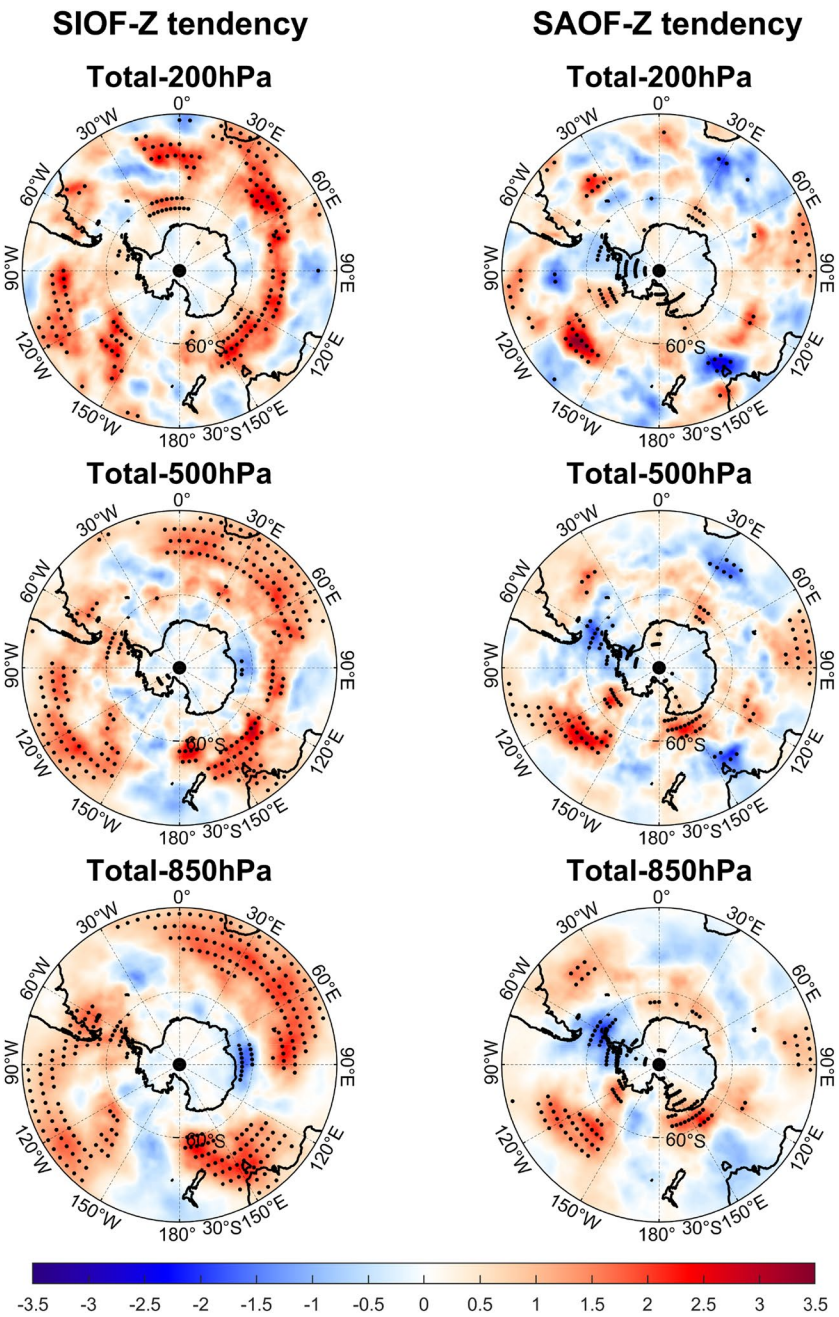

Fig. 12 Partial regressions of total geopotential height tendency (units: m/day) induced by the sum of transient eddy heating and vorticity forcings onto the normalized intensity indexes of SIOF (left), SAOF (right) at 200 hPa (top), 500 hPa (middle), and 850 hPa (bottom) in summer. And the intensity indexes are detrended before normalization. Black dots indicate the regions where the confidence level is larger than 95%

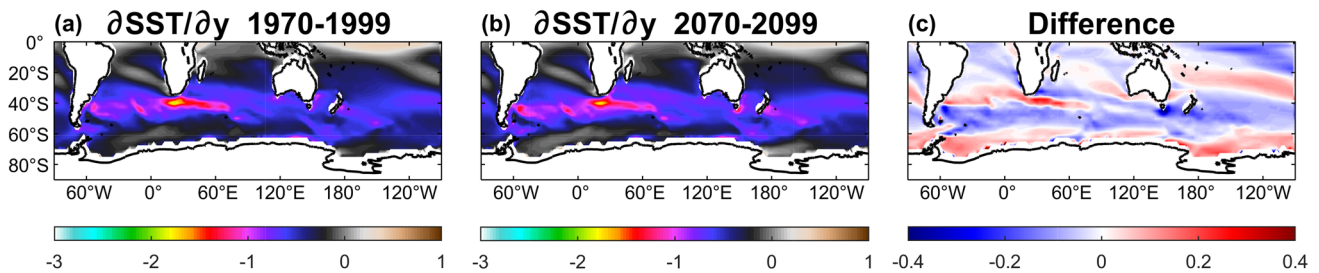

Fig. 13 **a** Multi-model mean SST meridional gradient (°C/100 km) during summer for 1970–1999. **b** Same as **a**, but for the future (2070–2099) climate. **c** Difference of multi-model mean SST meridional gradient (°C/100 km) between the future climate and the present-day

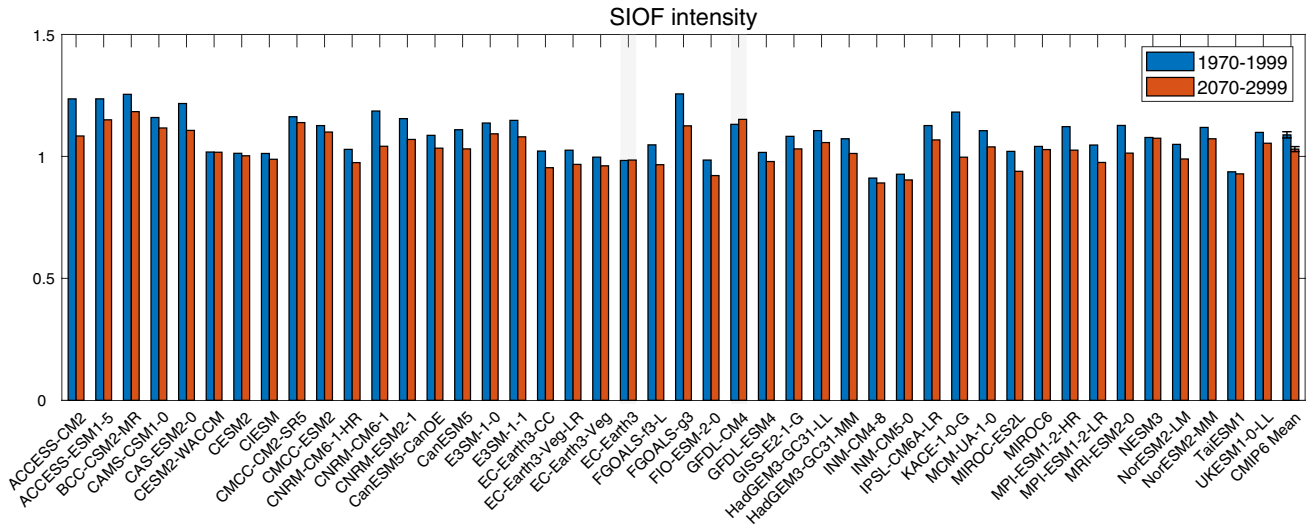

Fig. 14 A total of 42 out of the 44 models (95%) generate a decrease in SIOF intensity from the present-day (1970–1999, blue bars) to the future (2070–2099, red bars), with the exception of two models generating an increase (indicated by gray shading). The multi-model mean decrease of 5% is statistically significant above the 95% confidence level based on the bootstrap test. The error bar in the multi-model mean represents the 95% confidence level determined by a bootstrap test

SOF intensity is decreasing under global warming, with the greatest reduction occurring in the SIOF. To further verify it, we refer to the previous definition of the frontal intensity index, and use data from 44 CMIP6 models to obtain the SIOF intensity indexes for the periods 1970–1999 and 2070–2099. Then, we compare simulated SIOF intensity in these two periods. A total of 42 out of the 44 models (95%) simulate decreased intensity of SIOF (Fig. 14). The ensemble-mean shows a decrease of approximately 5% for frontal intensity, statistically significant above the 95% confidence according to a bootstrap test. The decreased SIOF intensity is in part forced by greenhouse warming, suggesting the impacts of SST fronts in SH on atmosphere are likely to reduce in the future and require further examination.

5.2 Relationships with atmospheric blockings

We note that the response of the atmospheric circulation to the SST front presents several high and low pressure centers, In fact, these structures can be connected with some specific atmospheric circulation patterns, such as the north–south dipole structure with a high pressure center at high latitudes and a low pressure center at low latitudes, corresponding to local atmospheric blockings, which cause local temperature changes and extreme weather (Che et al. 2021). It is worth to examine the relationship between the atmospheric dominant modes and atmospheric blockings with the SOF variability. For the two dominant modes in the extratropical atmospheric circulation in SH, namely the Southern Annular Mode (SAM) (Marshall 2003) and quasi-stationary zonal wave 3 (ZW3) pattern (Goyal et al. 2021), their relationship with SOF is weak, with correlation coefficients of 0.18 and 0.12, respectively.

We further investigate the impact of SOF variability on atmospheric blockings in SH. On the one hand, the total geopotential height tendency induced by transient eddies through 10–30 days band pass filter is calculated, which is the characteristic time scale associated with atmospheric blockings. The results show that the geopotential height tendency anomalies are relatively small (Fig. S4), indicating that the impact of eddy-forcing is weak. One the other hand, according to Cowan et al. (2013), we use the 500-hPa zonal wind U at subtropical and extratropical latitudes to define the atmospheric blocking index at each longitude in SH. A blocking index B at a given longitude is defined as

$$B = 0.5(U25^\circ S + U30^\circ S + U55^\circ S + U60^\circ S - U40^\circ S - U50^\circ S - 2 \times U45^\circ S).$$

This blocking definition describes the split of the westerly jet into two branches: a subtropical jet at 25°–30° S and a polar jet at 55°–60° S (Grose et al. 2012). The magnitude of this split can be quantified by the blocking index B, where positive values indicate the development of high (low) pressure systems in high-latitude (midlatitude) areas (Trenberth and Mo 1985). Then we calculate the correlation coefficients between the SOF intensity index and the blocking index B at each longitude, as shown in Fig. 15a. It can be seen that the correlation coefficient reaches its maximum in the South Pacific, up to 0.43, and the confidence level is larger than 95%, which is consistent with previous studies that midlatitude blocking is predominantly observed over

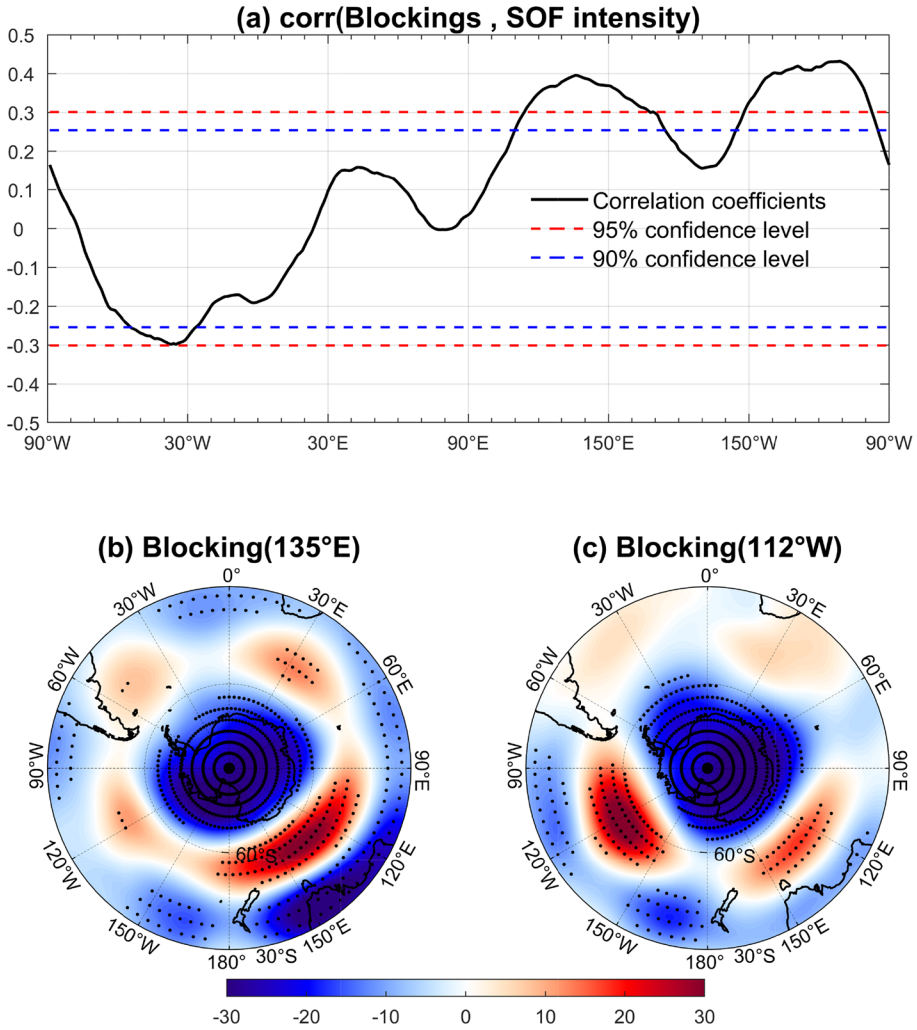

Fig. 15 **a** Correlation coefficients between the SOF intensity index and blocking index B at each longitude in summer. The red (blue) dashed line indicates that the correlation coefficients are significant at the 95% (90%) confidence level. **b**, **c** Regressions of 200-hPa geopotential height (units: m) onto the normalized blocking index B at longitudes **b** 135° E, **c** 112° W. Black dots indicate the regions where the confidence level is larger than 95%

the South Pacific (Sinclair 1996; Renwick and Revell 1999; Berrisford et al. 2007). The 200-hPa geopotential height anomalies regressed upon the blocking indices at 135° E and 112° W are shown in Fig. 15b, c, respectively. These atmospheric structures correspond to the atmospheric circulation induced by SOF (recall Fig. 8) and local atmospheric blockings, which can influence SH weather, being associated with heatwaves in New Zealand (Salinger et al. 2019) and Australia (Risbey et al. 2018), as well as persistent frost events in Australia (Risbey et al. 2019) and South America (Müller and Berri 2007).

5.3 Atmospheric responses to SST fronts diversity

As the SST frontal structure in the Southern Ocean is quite complex, the selection of frontal intensity should be approached with caution. To explore whether choosing other thresholds would make the results different, we choose 0.6 °C/100 km as the threshold to define the SAOF intensity index. Partial regressions of SST and storm track upon the new intensity index of SAOF are shown in Figs. S5 and S6, respectively. Compared with the results of choosing 0.8 °C/100 km as the threshold (Figs. 4b and 5b, e), there is no significant difference between the SST anomalies corresponding to the SIOF variability and the storm track anomalies induced by it (Figs. S5b and S6b, e). For the SAOF, however, it can be seen that the dipole structure of its corresponding SST anomalies has been enhanced and the boundaries of the SST positive and negative anomalies have been shifted northward. Although SST anomalies associated with the SAOF are larger at a threshold of 0.6 °C/100 km than at 0.8 °C/100 km, the responses of storm track are weaker compared to SIOF. That is, the SIOF variability still plays a dominant role in the influence of SST front variability on storm track in the Southern Ocean.

Note that the SAOF exhibits two peaks located on the poleward (SAOF1) and equatorward side (SAOF1), respectively. We further calculate the correlation coefficients between SAOF and SAOF1, SAOF2 based on different thresholds of 0.6 and 0.8 °C/100 km. When 0.8 °C/100 km

is selected as the threshold, the correlation between SAOF and SAOF1 as well as with SAOF2 are both strong (correlation coefficients are 0.68 and 0.58, respectively). When 0.6 °C/100 km is selected as the threshold, the correlation coefficient between SAOF and SAOF1 is as high as 0.9, while the coefficient with SAOF2 is only 0.29. We can infer that when the threshold is 0.8 °C/100 km, SAOF may reflect the combined effect of SAOF1 and SAOF2, whereas SAOF may mainly represent SAOF1 when the threshold is 0.6 °C/100 km, but their relative contribution needs to be further diagnosed in the future. Therefore, choosing 0.8 °C/100 km as the threshold is more reasonable without compromising the final results.

Our study focuses on the austral summer, which is when the intensity of SST fronts in the SH are strongest. However, the patterns of atmospheric responses and the relative contributions of different ocean basins may vary across seasons. For the atmospheric background, the westerly jet stream intensifies in spring, autumn, and winter, especially over the South Pacific (e.g., Nakamura and Shimpo 2004); meanwhile, from the downstream development perspective, wave packets in austral winter are less coherent than in austral summer (Lee and Held 1993). These factors are likely to lead to seasonal differences in the atmospheric response to SST fronts in different ocean basins. In this paper, the trends of SST fronts have been removed to focus on interannual variability, even though summer SST front displays an insignificant trend (Fig. 2). However, for other seasons, the long-term trends of SST fronts cannot be neglected, and the impacts of variations in SST fronts on the atmosphere might differ from interannual to decadal timescales. Furthermore, the Southern Ocean presents obvious multi-scale SST variations. In particular, the variability of mesoscale SSTs and their impacts on the mid-to-high latitude atmosphere remain largely unknown. The subsequent feedback of the atmosphere to multi-scale SSTs is also unclear. As low-resolution climate models are likely to underestimate the effect of air-sea interactions in mid-latitudes, future research needs to employ high-resolution climate models to further investigate these issues.

6 Summary

In this study, we characterize the variation of SST fronts in the Southern Ocean and the mid-latitude atmospheric response to frontal variabilities, especially the synoptic-scale eddy activities and eddy-driven atmospheric circulation. It has been found that large-scale SST fronts in the Southern Ocean exist throughout the year, with significant spatial differences and complex structures between basins. The most prominent fronts are concentrated at 60° W–120° E, which we define as the SOF, including the SIOF and SAOF. The SOF reaches its maximum intensity during austral summer (DJF), with a strong interannual variability and an insignificant trend. We then define frontal intensity indexes to quantitatively describe the intensity of SOF, SIOF and SAOF by using the zonally-averaged SST meridional gradients, respectively. On the interannual scale, the SST fronts in the Southern Ocean in summer have a significant impact on storm track activities in different tropospheres through atmospheric baroclinic processes, thereby modulating the variation of atmospheric circulation through eddy feedback mechanisms. When SST fronts intensify, the meridional air temperature gradient and atmospheric baroclinicity significantly increase, which in turns enhances the atmospheric baroclinic energy conversion and leads to stronger transient eddy activities. The transient eddies transport heat and vorticity fluxes, and the effects of transient eddy thermal and dynamical forcing on the seasonal-averaged atmospheric circulation differ considerably: the atmospheric responses to the transient eddy thermal forcing are baroclinic but to the transient eddy vorticity forcing are barotropic in vertical structure, and the overall atmospheric responses are dominated by the transient eddy vorticity forcing. The anomalous transient eddy activities ultimately tend to produce geopotential height anomalies as well as corresponding anomalous westerly jets with a barotropic structure over the whole SH. More importantly, SIOF variability dominates the response of storm track activities, especially in the downstream region, and modulates the anomalous response of the circumpolar atmospheric circulation through eddy feedback mechanism, whereas SAOF variability only produces limited local atmospheric response.

Supplementary Information The online version contains supplementary material available at https://doi.org/10.1007/s00382-023-07093-y.

Acknowledgements The authors thank the anonymous reviewers for their valuable comments and suggestions. This work is supported by National Natural Science Foundation of China (42376009) and National Key Research and Development Program of China (2019YFA0607001).

Author contributions All authors contributed to the study conception and design. Material preparation, data collection and analysis were performed by QR and LZ. The first draft of the manuscript was written by QR and all authors commented on previous versions of the manuscript. All authors read and approved the final manuscript.

Funding This work is supported by National Natural Science Foundation of China (Grant no. 42376009), National Key Research and Development Program of China (Grant no. 2019YFA0607001).

Data availability statement The ERA5 reanalysis dataset used for this study is available at https://www.ecmwf.int/en/forecasts/datasets/reanalysis-datasets/era5.

Declarations

Conflict of interest The authors declare that there is no conflict of interest.

Ethical approval Not applicable.

References

Berrisford P, Hoskins B, Tyrlis E (2007) Blocking and Rossby wave breaking on the dynamical tropopause in the Southern Hemisphere. J Atmos Sci 64(8):2881–2898

Cai M, Yang S, Van den Dool HM, Kousky VE (2007) Dynamical implications of the orientation of atmospheric eddies: a local energetics perspective. Tellus 59:127–140

Cai W et al (2023) Southern ocean warming and its climatic impacts. Sci Bull 68:946–960

Cayan DR (1992) Latent and sensible heat-flux anomalies over the northern oceans—the connection to monthly atmospheric circulation. J Clim 5:354–369

Chang EKM, Orlanski I (1993) On the dynamics of a storm track. J Atmos Sci 50:999–1015

Chang EKM, Lee S, Swanson KL (2002) Storm track dynamics. J Clim 15:2163–2183

Chapman CC, Lea MA, Meyer A, Sallée J, Hindell M (2020) Defining Southern Ocean fronts and their influence on biological and physical processes in a changing climate. Nat Clim Change 10(23):1–11

Che Z, Yao Y, Zhong L (2021) Wintertime sea surface temperature front around the Kuroshio Extension and its impact on North Pacific blocking. Int J Climatol 41(3):1905–1926

Chemke R, Ming Y, Yuval J (2022) The intensification of winter mid-latitude storm tracks in the Southern Hemisphere. Nat Clim Change 12(6):1–5

Chen QY, Hu HB, Ren XJ, Yang XQ (2019) Numerical simulation of midlatitude upper-level zonal wind response to the change of North Pacific subtropical front strength. J Geophy Res Atmos 124(9):4891–4912

Cowan T, Van Rensch P, Purich A, Cai W (2013) The association of tropical and extratropical climate modes to atmospheric blocking across southeastern Australia. J Clim 26(19):7555–7569

Czaja A, Frankignoul C (1999) Influence of the North Atlantic SST on the atmospheric circulation. Geophys Res Lett 26:2969–2972

Deser C, Blackman M (1993) Surface climate variations over the North Atlantic Ocean during winter: 1900–1989. J Clim 6:1743–1753

Durack PJ, Gleckler PJ, Landerer FW, Taylor KE (2014) Quantifying underestimates of long-term upper-ocean warming. Nat Clim Change 4(11):999–1005

Eady ET (1949) Long waves and cyclone waves. Tellus 1:33–52

Eyring V et al (2016) Overview of the Coupled Model Intercomparison Project Phase 6 (CMIP6) experimental design and organization. Geosci Model Dev 9(5):1937–1958

Fang J, Yang XQ (2016) Structure and dynamics of decadal anomalies in the wintertime midlatitude North Pacific ocean–atmosphere system. Clim Dyn 47:1989–2007

Frankignoul C, Sennéchael N, Kwon Y, Alexander M (2011) Influence of the meridional shifts of the Kuroshio and the Oyashio Extensions on the atmospheric circulation. J Clim 24:762–777

Freeman NM, Lovenduski NS, Gent PR (2016) Temporal variability in the Antarctic Polar Front (2002–2014). J Geophy Res Oceans 121(10):7263–7276

Goyal R, Jucker M, Sen Gupta A, Hendon HH, England MH (2021) Zonal wave 3 pattern in the Southern Hemisphere generated by tropical convection. Nat Geosci 14(10):732–738

Graham RM, de Boer AM, Heywood KJ, Chapman MR, Stevens DP (2012) Southern Ocean fronts: controlled by wind or topography? J Geophys Res Oceans 117:C08018

Grose MR, Pook MJ, McIntosh PC, Risbey JS, Bindoff NL (2012) The simulation of cutoff lows in a regional climate model: reliability and future trends. Clim Dyn 39:445–459

Hopkins J, Challenor P, Shaw AGP (2008) A new statistical modeling approach to ocean front detection from SST satellite images. J Atmos Ocean Technol 27(1):173–191

Hoskins J, Hodges KI (2005) A new perspective on Southern Hemisphere storm tracks. J Clim 18(20):4108–4129

Kostianoy AG, Ginzburg AI, Frankignoulle M, Delille B (2004) Fronts in the Southern Indian Ocean as inferred from satellite sea surface temperature data. J Mar Syst 45(1–2):55–73

Kushnir Y, Robinson WA, Blade I, Hall NMJ, Peng S, Sutton R (2002) Atmospheric GCM response to extratropical SST anomalies: synthesis and evaluation. J Clim 15:2233–2256

Kuwano-Yoshida A, Minobe S (2017) Storm track response to SST fronts in the Northwestern Pacific region in an AGCM. J Clim 30:1081–1102

Kwon YO, Alexander MA, Bond NA, Frankignoul C, Nakamura H, Qiu B, Thompson LA (2010) Role of the Gulf Stream and Kuroshio–Oyashio systems in large-scale atmosphere–ocean interaction: a review. J Clim 23:3249–3281

Lau NC, Holopainen E (1984) Transient eddy forcing of the time mean flow as identified by geopotential tendencies. J Atmos Sci 41:313–328

Lee S, Held IM (1993) Baroclinic wave packets in models and observations. J Atmos Sci 50:1413–1428

Lee S, Kim HK (2003) The dynamical relationship between subtropical and eddy-driven jets. J Atmos Sci 60(12):1490–1503

Levitus S, Antonov J, Boyer T (2005) Warming of the world ocean 1955–2003. Geophys Res Lett 32:L02604

Lim EP, Simmonds I (2002) Explosive cyclone development in the Southern Hemisphere and a comparison with Northern Hemisphere events. Mon Weather Rev 130(9):2188–2209

Lindzen RS, Farrell BF (1980) A simple approximation result for maximum growth rate of baroclinic instabilities. J Atmos Sci 37:1648–1654

Lorenz DJ, Hartmann DL (2001) Eddy–zonal flow feedback in the Southern Hemisphere. J Atmos Sci 58(21):3312–3327

Mantua NJ, Hare SR (2002) The Pacific decadal oscillation. J Oceanogr 58:35–44

Mantua NJ, Hare SR, Zhang Y, Wallace JM, Francis RC (1997) A Pacific interdecadal climate oscillation with impacts on salmon production. Bull Am Meteorol Soc 78:1069–1079

Marshall GJ (2003) Trends in the Southern Annular Mode from observations and reanalyses. J Clim 16(24):4134–4143

Minobe SA, Kuwano-Yoshida A, Komori N, Xie SP, Small RJ (2008) Influence of the Gulf Stream on the troposphere. Nature 452:206–209

Moore JK, Abbott MR, Richman JG (1999) Location and dynamics of the Antarctic Polar Front from satellite sea surface temperature data. J Geophys Res Oceans 104(C2):3059–3073

Müller GV, Berri GJ (2007) Atmospheric circulation associated with persistent generalized frosts in Central-Southern South America. Mon Weather Rev 135:1268–1289

Nakamura H, Shimpo A (2004) Seasonal variations in the Southern Hemisphere storm tracks and jet streams as revealed in a reanalysis dataset. J Clim 17(9):1828–1844

Nakamura M, Yamane S (2010) Dominant anomaly patterns in the near-surface baroclinicity and accompanying anomalies in the atmosphere and oceans. Part II: North Pacific basin. J Clim 23(24):6445–6467

Nakamura H, Sampe T, Tanimoto Y, Shimpo A (2004) Observed associations among storm tracks, jet streams and midlatitude oceanic fronts. Earths Clim Ocean Atmos Interact Geophys Monogr 147:329–345

Nakamura H, Sampe T, Goto A, Ohfuchi W, Xie SP (2008) On the importance of midlatitude oceanic frontal zones for the mean state and dominant variability in the tropospheric circulation. Geophys Res Lett 35(15):971–978

Nakayama M, Nakamura H, Ogawa F (2021) Impacts of a midlatitude oceanic frontal zone for the baroclinic annular mode in the Southern Hemisphere. J Clim 34:7389–7408

Namias J, Cayan DR (1981) Large-scale air–sea interactions and short period climate fluctuations. Science 214:869–876

Nishii K, Nakamura H, Miyasaka T (2009) Modulations in the planetary wave field induced by upward-propagating Rossby wave packets prior to stratospheric sudden warming events: a case-study. Q J R Meteorol Soc 135:39–52

Nonaka M, Nakamura H, Taguchi B, Komori N, Kuwano-Yoshida A, Takaya K (2009) Air–sea heat exchanges characteristic of a prominent midlatitude oceanic front in the south Indian Ocean as simulated in a high-resolution coupled GCM. J Clim 22:6515–6535

O'Reilly C, Czaja A (2015) The response of the Pacific storm track and atmospheric circulation to Kuroshio extension variability. Q J R Meteorol Soc 141:52–66

O'Reilly C, Minobe S, Kuwano-Yoshida A, Woollings T (2017) The Gulf Stream influence on wintertime North Atlantic jet variability. Q J R Meteorol Soc 143:173–183

Ogawa F, Nakamura H, Nishii K, Miyasaka T, Kuwano-Yoshida A (2012) Dependence of the climatological axial latitudes of the tropospheric westerlies and storm tracks on the latitude of an extratropical oceanic front. Geophys Res Lett 39:L05804

Ogawa F, Nakamura H, Nishii K, Miyasaka T, Kuwano-Yoshida A (2016) Importance of midlatitude oceanic frontal zones for the annular mode variability: interbasin differences in the southern annular mode signature. J Clim 29:6179–6199

Orlanski I, Chang EKM (1993) Ageostrophic geopotential fluxes in downstream and upstream development of baroclinic waves. J Atmos Sci 50(2):212–225

Parfitt RA, Czaja S, Minobe K-Y (2016) The atmospheric frontal response to SST perturbations in the Gulf Stream region. Geophys Res Lett 43(5):2299–2306

Ren X, Li Z, Cai W, Li X, Wang CY, Jin Y, Wu L (2022) Influence of tropical Atlantic meridional dipole of sea surface temperature anomalies on Antarctic autumn sea ice. Environ Res Lett 17:094046

Renwick JA, Revell MJ (1999) Blocking over the South Pacific and Rossby wave propagation. Monthly Weather Rev 127(10):2233–2247

Risbey JS, O'Kane TJ, Monselesan DP, Franzke CL, Horenko I (2018) On the dynamics of austral heat waves. J Geophys Res Atmos 123(1):38–57

Risbey JS, Monselesan DP, O'Kane TJ, Tozer CR, Pook MJ, Hayman PT (2019) Synoptic and large-scale determinants of extreme austral frost events. J Appl Meteorol Climatol 58(5):1103–1124

Robinson WA (2006) On the self-maintenance of midlatitude jets. J Atmos Sci 63(8):2109–2122

Salinger MJ et al (2019) The unprecedented coupled ocean-atmosphere summer heatwave in the New Zealand region 2017/18: drivers, mechanisms and impacts. Environ Res Lett 14(4):044023

Sampe T, Nakamura H, Goto A, Ohfuchi W (2010) Significance of a midlatitude SST frontal zone in the formation of a storm track and an eddy-driven westerly jet. J Clim 23:1793–1814

Simmonds I, Keay K (2000) Variability of Southern Hemisphere extratropical cyclone behavior, 1958–97. J Clim 13(3):550–561

Sinclair MR (1996) A climatology of anticyclones and blocking for the Southern Hemisphere. Monthly Weather Rev 124(2):245–264

Small RJ, Tomas RA, Bryan FO (2014) Storm track response to ocean fronts in a global high-resolution climate model. Clim Dyn 43(3–4):805–828

Taguchi B, Nakamura H, Nonaka M, Xie SP (2009) Influences of the Kuroshio/Oyashio extensions on air–sea heat exchanges and storm-track activity as revealed in regional atmospheric model simulations for the 2003/04 cold season. J Clim 22(24):6536–6560

Taguchi B, Nakamura H, Nonaka M, Komori N, Kuwano-Yoshida A, Takaya K, Goto A (2012) Seasonal evolutions of atmospheric response to decadal SST anomalies in the North Pacific subarctic frontal zone: observations and a coupled model simulation. J Clim 25:111–139

Trenberth KF, Mo KC (1985) Blocking in the southern hemisphere. Mon Weather Rev 113(1):3–21

Wang L, Hu H, Yang X (2019) The atmospheric responses to the intensity variability of subtropical front in the wintertime North Pacific. Clim Dyn 52:5623–5639

Wijffels S, Roemmich D, Monselesan D, Church J, Gilson J (2016) Ocean temperatures chronicle the ongoing warming of Earth. Nat Clim Change 6(2):116–118

Wills SM, Thompson DWJ (2018) On the observed relationships between wintertime variability in Kuroshio–Oyashio Extension sea surface temperature and the atmospheric circulation over the North Pacific. J Clim 31:4669–4681

Yin H (2005) A consistent poleward shift of the storm tracks in simulations of 21st century climate. Geophys Res Lett 32:L18701

Zhang R, Fang J, Yang XQ (2020a) What kinds of atmospheric anomalies drive wintertime north pacific basin-scale subtropical oceanic front intensity variation? J Clim 33(16):7011–7026

Zhang L, Gan B, Wang H, Wu L, Cai W (2020b) Essential role of the midlatitude South Atlantic variability in altering the Southern Hemisphere summer storm tracks. Geophys Res Lett 47:e2020GL087910

Zhang L, Gan B, Li X, Wang H, Wang C, Cai W, Wu L (2021) Remote influence of the midlatitude South Atlantic variability in spring on Antarctic summer sea ice. Geophys Res Lett 48:e2020GL090810

Zhang L, Ren X, Wang CY, Gan B, Wu L, Cai W (2023) An observational study on the interactions between storm tracks and sea ice in the Southern Hemisphere. Clim Dyn 62:17–36